Journal of
Materials Chemistry A

ROYAL SOCIETY
OF CHEMISTRY

PAPER

View Article Online
View Journal | View Issue

Cite this: *J. Mater. Chem. A*, 2023, **11**, 17101

Ultrahigh photoresponse in strain- and domain-engineered large-scale MoS_2 monolayer films†

Ye Seul Jung,[a] Jae Woo Park,[ab] Ji Yeon Kim,[a] Youngseo Park,[c] Dong Gue Roe,[d] Junseok Heo,[c] Jeong Ho Cho[e] and Yong Soo Cho*[a]

Strain engineering has been recognized as a critical strategy for controlling electrical and optoelectronic properties, even in atomically thick two-dimensional (2D) transition metal dichalcogenides. Herein, the combined effects of strain engineering and domain engineering are explored in unconventional centimeter-scale monolayer MoS_2 films to generate ultrahigh photoresponses. Two-step strain engineering for maximizing the built-in tensile strain favorably reduced the optical bandgap of monolayer MoS_2 and the potential barriers at junctions, resulting in record performance. Directional adjustments of the domains with respect to their atomic arrangement in the planar epitaxial structure of MoS_2 also contributed to the extraordinary photodetection behavior. As a performance highlight, an impressive photocurrent of 22.9 μA and photoresponsivity of 1142 A W^{-1} at an incident power density of 9×10^{-4} mW cm^{-2} were achieved in the case of a total tensile strain of +1.80% and domain adjustment with zigzag-edge atomic arrays, which are the highest values reported thus far for 2D visible photodetectors. The origin of these enhancements is systematically examined with experimental evidence, including changes in the energy bandgap and estimated potential barriers associated with band alignments and an additional polarization field.

Received 4th February 2023
Accepted 10th April 2023

DOI: 10.1039/d3ta00642e

rsc.li/materials-a

Introduction

Strain engineering has emerged as a powerful pathway for modulating the electrical, optical, and mechanical properties of inorganic materials, thus enhancing their performance in electronic and optoelectronic devices.[1–3] In particular, two-dimensional (2D) layered materials have attracted considerable attention for flexible optoelectronics owing to their sub-nanometer thickness, uniquely confined structure, and various appealing optoelectronic properties with ultrahigh strain tenability.[4–7] The effects of strain on the phonon structure, energy band structure, transport behavior, interfacial characteristics, and optoelectronic properties of 2D semiconductors have been extensively investigated through both experiments and simulations.[8–11] In particular, recognizing their strain-sensitive optoelectronic properties, several researchers have endeavored to experimentally adopt strain engineering to improve their photodetection behavior for 2D photodetectors.[12–14]

Most reported studies on the strain engineering of 2D transition metal dichalcogenides (TMDs) have imposed additional strain in the range of −0.62% to +1.4% by either mechanically bending or stretching micrometer-scale single-crystal 2D layers subsequently transferred onto flexible polymer substrates.[15–18] In addition, a wrinkled/crumpled state was intentionally created by releasing a stretched 2D layer on an elastomer substrate, and the strain-dependent sensitivity of the optoelectronic parameters was examined.[14,19] However, all of the strain-dependent characteristics were investigated in a limited manner while maintaining the bent state (and thus, not in the flat state). For example, when a post-bending tensile strain of +0.65% was applied to an In_2Se_3 nanosheet, its photoresponsivity R was found to have increased to 0.37 A W^{-1}, which was approximately 1.68-fold higher than that of a flat unstrained nanosheet.[20] A single-crystal MoS_2 monolayer was also reported to exhibit an enhanced photocurrent I_{ph} of 0.21 μA under −0.38% strain.[13] The reported improvements in the photoresponse of TMD photodetectors were due to the lowered barrier height caused by a positive polarization potential, which was induced by the electromechanical coupling of piezoelectric TMD materials under mechanical bending.[21] Therefore, because of the *in situ* strain engineering of TMDs in the flat

---

[a] *Department of Materials Science and Engineering, Yonsei University, Seoul 03722, Republic of Korea. E-mail: ycho@yonsei.ac.kr*
[b] *Samsung Electronics Co. Ltd, Gyeonggi-do 16677, Republic of Korea*
[c] *Department of Electrical and Computer Engineering, Ajou University, Suwon 16499, Republic of Korea*
[d] *School of Electrical and Electronic Engineering, Yonsei University, Seoul 03722, Republic of Korea*
[e] *Department of Chemical and Biomolecular Engineering, Yonsei University, Seoul 03722, Republic of Korea*

† Electronic supplementary information (ESI) available. See DOI: **https://doi.org/10.1039/d3ta00642e**

state, the mechanism of strain-dependent photodetection must be different, which has not been reported thus far.

Herein, we introduce an unprecedented *in situ* processing method for intentionally imposing controllable strain in large-scale monolayer MoS_2 films on a polyethylene terephthalate (PET) substrate, primarily aiming to enhance the photoresponse in the flat state. This *in situ* method can induce compressive or tensile strain within the crystal lattice (reaching a strain level up to $\pm1.27\%$) prior to adjusting the specific domain orientation. Strain with a negative (positive) sign is compressive (tensile) strain. The magnitude of the built-in tensile or compressive *in situ* strain was determined by the bending curvature of the substrate while transferring large-scale MoS_2 onto the substrate, which was applied in either a concave or convex manner. A maximum tensile strain of +1.27% increased the photoresponsivity of a centimeter-scale MoS_2 monolayer and decreased the optical bandgap from 1.83 to 1.78 eV. To further increase the tensile strain, additional post-bending was applied to strained 2D materials. As expected, this double-strain engineering approach resulted in an even higher R of 1142 A W^{-1} with a maximum total strain of +1.80%, which was nearly 129.3 times higher than that of the unstrained reference sample. This value is higher than all values reported thus far for visible or flexible photodetectors based on 2D materials.

These excellent achievements were also a consequence of the domain alignment in the planar epitaxial grain structure of large-scale MoS_2, which was adjusted by positioning parallel electrodes with specific angles for maximum electromechanical coupling. Although the fundamental relationship between the atomic arrangement, *i.e.*, zigzag *versus* armchair atomic arrays, and the piezoelectricity generated under mechanical stimuli is well known.[21–25] This study introduces, for the first time, domain adjustments in large-scale monolayer TMD films (rather than previously reported single-crystal triangles with dimensions of a few tens of micrometers) for optimal photodetection behavior. Such TMD photodetectors based on monolayer films have never been reported because the synthesis of high-quality large-scale 2D monolayers with controlled preferential domains has been limited. The origin of the strain-dependent enhancements in a lateral monolayer MoS_2 photodetector, which incorporates specific electrode positioning relative to the atomic arrays, is explored systematically with experimental evidence of the modulated optical bandgap and estimated potential barriers.

Results and discussion

Large-scale synthesis and *in situ* strain engineering of MoS_2 monolayer films

Fig. 1a schematically shows the critical steps involved in executing the double-strain engineering of large-scale monolayer MoS_2 films. Prior to the *in situ* straining process, large-scale monolayer MoS_2 films were synthesized on a sapphire substrate *via* low-pressure chemical vapor deposition (LPCVD) with the assistance of a unique Na_2S growth promotor, as reported in our previous study.[26] A photograph of the synthesized large-scale MoS_2 monolayer film with dimensions of ∼15 × 15 mm is shown in the inset of Fig. 1a. As shown in the experimental set-up for the chemical vapor deposition (CVD) synthesis process in Fig. S1 of the ESI,† the successful formation of a large-scale monolayer was enabled by this Na_2S growth promotor, which also passivated sulfur vacancies. As reported previously by our group,[26] the growth mechanism of MoS_2 under the presence of Na_2S likely differs from the typical reaction between MoO_3 and S precursors. Because Na evaporates earlier according to the Born–Haber cycle, gas-phase Na reacts with MoO_3 powder to form $NaMoO_{3-x}$. The potential $NaMoO_{3-x}$ phase may facilitate the nucleation of MoS_2 with the supply of sulfur at the growth temperature. The synthesized MoS_2 film was confirmed to have uniform monolayer coverage with no discrete single crystals by multiple characterization results, including optical microscopy (Fig. S2 (ESI†)), an atomic force microscopy (AFM) image showing a step height of ∼0.89 nm (Fig. S3 (ESI†)), and Raman mapping over the large-area film (Fig. S4 (ESI†)). A high-angle annular dark-field scanning transmission electron microscopy (HAADF-STEM) image and the corresponding fast Fourier transform selected-area electron diffraction (FFT-SAED) pattern (Fig. S5 (ESI†)) further confirm the high quality of the MoS_2 and the absence of sulfur vacancies. Additional Raman and photoluminescence (PL) spectra at nine different spots in the centimeter-scale MoS_2 film are also shown in Fig. S6 (ESI†), indicating the fairly good coverage of the monolayer film.

Next, the synthesized large-scale film was spin-coated with poly(methyl methacrylate) (PMMA) and annealed at 80 °C for 10 min. After separating from the substrate, the PMMA/MoS_2 sample floated on the surface of water and was scooped up by a PET substrate pre-bent concavely or convexly. The detailed steps of the synthesis and transfer are illustrated in Fig. S7 (ESI†). Pre-bending the polymer substrate is key to imposing the additional *in situ* lattice strain in MoS_2. For example, a concavely (or convexly) bent substrate provides tensile (or compressive) strain when the flat state of the MoS_2 film is recovered. The magnitude of the compressive or tensile strain was controlled by applying different bending curvatures to the substrate, where a smaller curvature induced a larger strain. The *in situ* pre-strain ε_i used here ranged from -1.27% to $+1.27\%$. The procedure for calculating ε_i is shown in Fig. S8 (ESI†). After removing the PMMA layer with acetone, two-terminal photodetectors based on the monolayer MoS_2 films were fabricated by the thermal evaporation of Ni/Au (2 nm/50 nm in thickness) electrodes, which were carefully aligned relative to the domain orientation of MoS_2. To observe the effect of extended strain, the photodetector was also post-bent out in a convex manner to generate a maximum strain of up to +2.54%.

Fig. 1b shows a lateral force microscopy (LFM) image of a synthesized 50 × 50 μm monolayer film, which is color-coded to visualize the domain orientations. LFM detects the difference in lateral deflections as electrical signals when the tip scans across the grain boundary.[27,28] The film exhibited regions of only two specific domain structures with relative orientation angles, θ, of 0° (pink) and 60° (violet). These domains have a 180° relation (*i.e.*, mirror symmetry) and are thus identical atomic

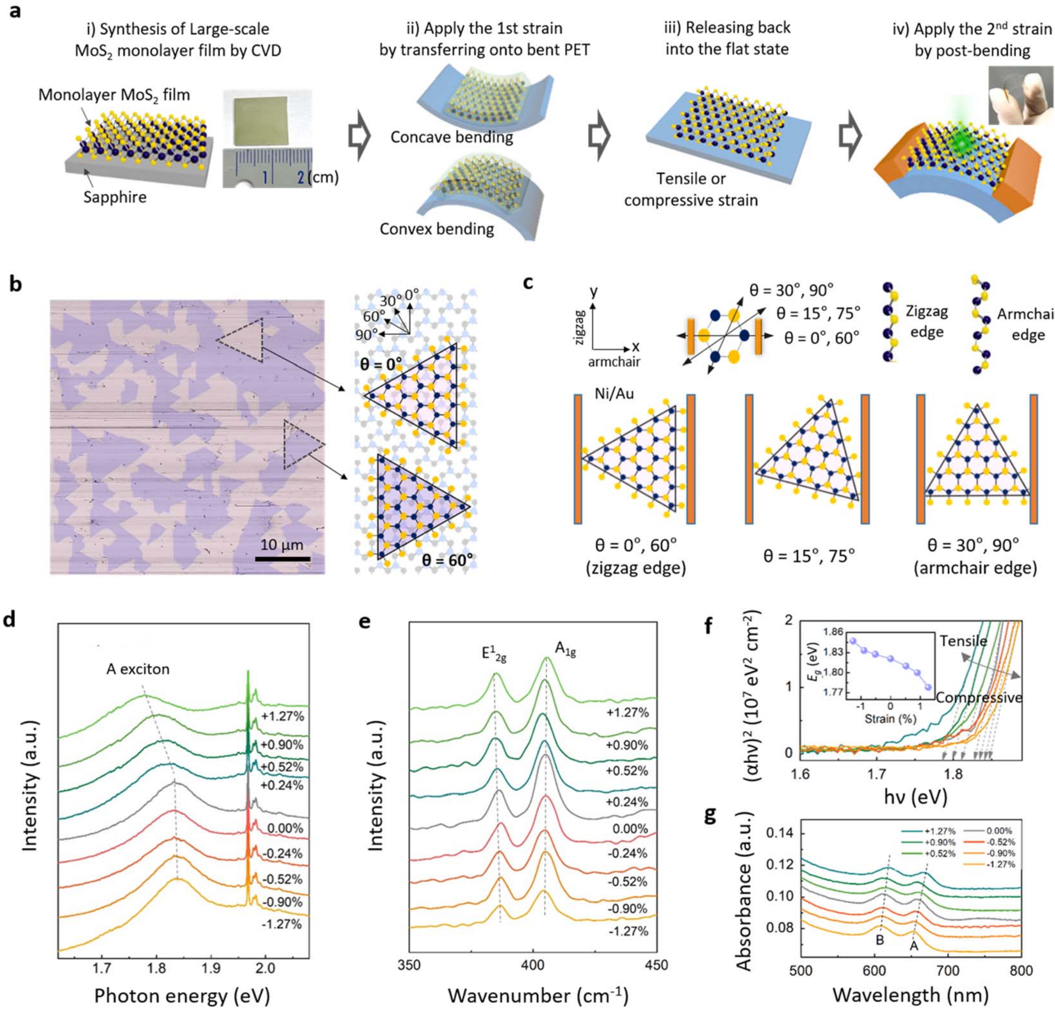

Fig. 1 (a) Schematic illustration of the double-strain engineering process consisting of (i) the LPCVD synthesis of a large-scale MoS_2 monolayer film, (ii) transferring the MoS_2 film onto a concavely or convexly pre-bent PET substrate for the first strain engineering with ±1.27% strain, (iii) releasing the film back to the flat state, and (iv) post-bending process the pre-bent sample for the second strain engineering up to ±2.54%; left inset: photograph of a synthesized centimeter-scale MoS_2 film on a sapphire substrate and right inset: photograph of a flexible transparent MoS_2 photodetector on a PET substrate. (b) LFM image of the MoS_2 monolayer showing a domain structure consisting of merged single-crystal flakes in two dominant orientations colored pink and violet as a visual aid, corresponding to orientation angles of θ of 0° and 60°, respectively, on the background atomic structure of a *c*-plane sapphire substrate. (c) Three different electrode configurations relative to the domain orientations: 0° (or 60°) domain, 15° (or 75°) domain, and 30° (or 90°) domain electrodes. (d) PL spectra and (e) Raman spectra of the MoS_2 films processed with *in situ* strain ε_i in the range of −1.27 to +1.27%, showing obvious peak shifts with applied ε_i. (f) Plots of $(\alpha\hbar\nu)^2$ *versus* $\hbar\nu$ for the strained MoS_2 films from the UV-visible spectra, representing changes in the optical absorption edges with ε_i, inset: variation in the optical bandgap as a function of ε_i. (g) Absorbance spectra of the strained MoS_2 films, confirming the presence of lattice strain caused by the *in situ* strain transfer process.

arrangements. The two opposite 0°- and 60°-oriented domains were almost equally distributed, accounting for 50.8% and 49.2% of the domains, respectively. The preferred growth is the result of a minimal lattice mismatch with the *c*-plane (0001) sapphire substrate, whereas growth on the Si substrate usually leads to the random growth of triangular domains.[26,29,30] The electrodes were directionally adjusted according to the domain structure of the monolayer film in three different ways, as illustrated in Fig. 1c. Specifically, 0° (or 60°)-, 15° (or 75°)-, and 30° (or 90°)-oriented electrodes were positioned parallel to the specific atomic arrangements. The 0° (or 60°)- and 30° (or 90°)-oriented electrodes specifically correspond to the zigzag-edge and armchair-edge terminations of the atomic arrays, respectively (Fig. 1c).

We initially recorded the strain-dependent PL spectra of the *in situ* prestrained MoS_2 monolayer films, as shown in Fig. 1d. The prominent A exciton peak observed at 1.83 eV for the unstrained sample suggests the presence of a direct bandgap. The PL peak apparently shifted from ∼1.83 to ∼1.75 eV with the increasing ε_i in the tensile region, whereas it shifted slightly from ∼1.83 to ∼1.85 eV with increasing compressive strain. Fig. 1e presents the ε_i-dependent Raman spectra of the MoS_2 monolayer. As is typical for monolayer MoS_2, the Raman spectra displayed two distinguishable peaks for all cases, *i.e.*, an E^1_{2g} peak (in-plane vibration) at 386.2 cm^{-1} and an A_{1g} peak (out-of-plane vibration) at 404.7 cm^{-1}.[16] The A_{1g} peak position remained relatively unchanged with variations in ε_i, whereas the E^1_{2g} peak distinctly shifted toward lower wavenumbers with increasing ε_i, particularly in the tensile region. The stronger ε_i-dependent changes in the E^1_{2g} peak indicate that the built-in strain influences the MoS_2 lattice in the in-plane direction more than it does in the out-of-plane direction.[16,31] As anisotropic lattice changes are expected with *in situ* strain, the out-of-plane extension is likely to be limited by the compressive strain applied in the in-plane direction because of the nature of the monolayer structure.

The spectral transmittance and reflectance curves of the MoS_2 film were obtained using ultraviolet (UV)-visible spectroscopy, primarily to define the ε_i-dependent optical bandgap. This may be the first time the optical bandgap of monolayer films has been measured, which was previously not possible because of the typical sample size of a few tens of micrometers. Fig. 1f shows plots of $(\alpha\hbar\nu)^2$ *versus* photon energy $\hbar\nu$, where $\hbar$ is the Planck constant, ν is the wavelength of the incident light, and α is the absorption coefficient. The optical bandgap E_g was estimated from Tauc's relationship by extrapolating the curves to the x-axis.[32,33] The absorption edge of each strained sample exhibited clear red shifts with increasing ε_i toward the tensile region, as demonstrated by the change in E_g in the inset of Fig. 1f. In addition, the bandgap decreased from 1.85 to 1.78 eV over the ε_i range from −1.27 to +1.27%. The maximum E_g difference of ~0.069 eV is very similar to the change of 0.071 eV estimated from the shift in the A exciton peak in the PL spectra shown in Fig. 1d. Fig. 1g shows the optical absorbance spectra as a function of the excitation wavelength of all samples, which were extracted from the transmittance and reflectance curves. Two excitonic transitions at wavelengths of ~618 and ~670 nm were identified in the ε_i-dependent spectra, which were associated with the B- and A-interband transitions, respectively, at the K point of the Brillouin zone of MoS_2.[34,35] As expected, both the B and A exciton peaks red-shifted with increasing ε_i over the compressive-to-tensile strain region, confirming the narrowing of the MoS_2 bandgap.

Photodetection performance of *in situ* strained MoS_2 monolayer

The effects of the presence of compressive and tensile ε_i were verified by characterizing the photodetection performance of large-scale monolayer-MoS_2-based photodetectors with an active area of 100 μm × 50 μm for 0° (or 60°)-domain-oriented Ni/Au electrodes. Note that a photomask was used for the electrode patterning, which is a merit of large-scale sample not necessitating the photolithography or e-beam lithography. An optical image showing the channel length of ~100 μm is seen in Fig. S9 (ESI†). Fig. 2a and b shows the photocurrent I_{ph} *versus* time at a source-drain voltage (V_{sd}) of +10 V for the monolayer film processed with compressive and tensile ε_i under a 532 nm laser. The irradiation was focused onto a spot with a diameter of ~1.2 mm for a laser power density of 259 mW cm^{-2}. I_{ph} was determined from the relation $I_{on} - I_{off}$, where I_{on} and I_{off} are the I_{sd} (source-drain currents) in the on and off states, respectively. On/off switching was clearly observed; specifically, I_{ph} was suddenly detected in the on-state under illumination and was extinguished in the off-state with no illumination. The I_{ph} value gradually increased over the compressive-to-tensile strain region. Fig. 2c shows the photocurrent I_{ph} of all the strained devices with applied V_{sd} of +1, +5, and +10 V. Evidently, I_{ph} strongly depended on ε_i, as a higher I_{ph} was predominantly observed, especially in the tensile region. I_{ph} also increased with increasing V_{sd}, owing to the accompanying higher drift velocity and shorter transit time.[36,37] An impressive I_{ph} value of ~19.2 μA was attained at +10 V for the +1.27%-strained sample, in contrast to ~2.4 and ~0.37 μA for the unstrained reference and −1.27%-strained samples, respectively. Fig. S10 (ESI†) presents the dependence of the light power density P on I_{ph} in the P range of 85 to 259 mW cm^{-2}, indicating that I_{ph} increased linearly with increasing P for all strains, as expected.[37,38] The ε_i-dependent electrical transport behavior of I_{sd}–V_{sd} was also characterized by sweeping the bipolar voltage V_{sd} swept from −5 to +5 V, as presented in Fig. S11 (ESI†). I_{sd} strongly depended on the applied ε_i, as was evident from the gradual decrease in I_{sd} with the increasing compressive strain and the higher I_{sd} with the increasing tensile strain, *e.g.*, I_{sd} of 0.47, 2.53, and 20.82 μA at +5 V for $\varepsilon_i = -1.27\%$, 0%, and +1.27%, respectively.

Fig. 2d schematically shows the band structure of the photodetectors for the cases of compressive and tensile ε_i with the application of V_{sd}, which reflects the ε_i-dependent changes in the optical bandgap and Fermi level of MoS_2. Schottky barriers are believed to form when MoS_2 comes into contact with Au on each side owing to the difference in the work function Φ.[39,40] The formation of Schottky junctions at each electrode contact is expected from the reported difference in Φ between MoS_2 (4.48 eV)[39] and Au (5.2 eV).[40] The resultant Schottky junctions create a barrier height φ at each junction with equilibrated Fermi levels through the photodetector structure. Applying a positive V_{sd} to the source electrode induces a potential energy difference across the MoS_2 layer, resulting in a gradient in the Fermi level. The change in the work function with compressive or tensile ε_i was estimated by measuring the contact potential of the strained MoS_2 relative to the substrate using Kelvin probe force microscopy (KPFM), as reported previously.[41,42] As shown in Fig. 2e, relative to 53.5 meV for the unstrained MoS_2, +1.27% strain increased the potential difference to 75.8 meV, whereas −1.27% strain lowered it to 44.7 meV. These contact potential differences indicate changes in the Fermi level of MoS_2 in the presence of *in situ* strain. For example, tensile strain is likely to lower the Fermi level of MoS_2 by increasing the work function, thereby reducing the barrier height at the Schottky junctions, because a larger potential difference was observed by KPFM. Therefore, both the lowered barrier height at the Schottky contacts and the applied V_{sd} facilitate charge transport toward the electrodes on each side, particularly in the tensile strain case. The photoresponse under illumination is also intensified with the reduced optical bandgap (~1.78 eV) and thus higher generation rates of electron–hole pairs in the tensile strain case. The opposite situation is anticipated for the compressive-strain case: a higher barrier

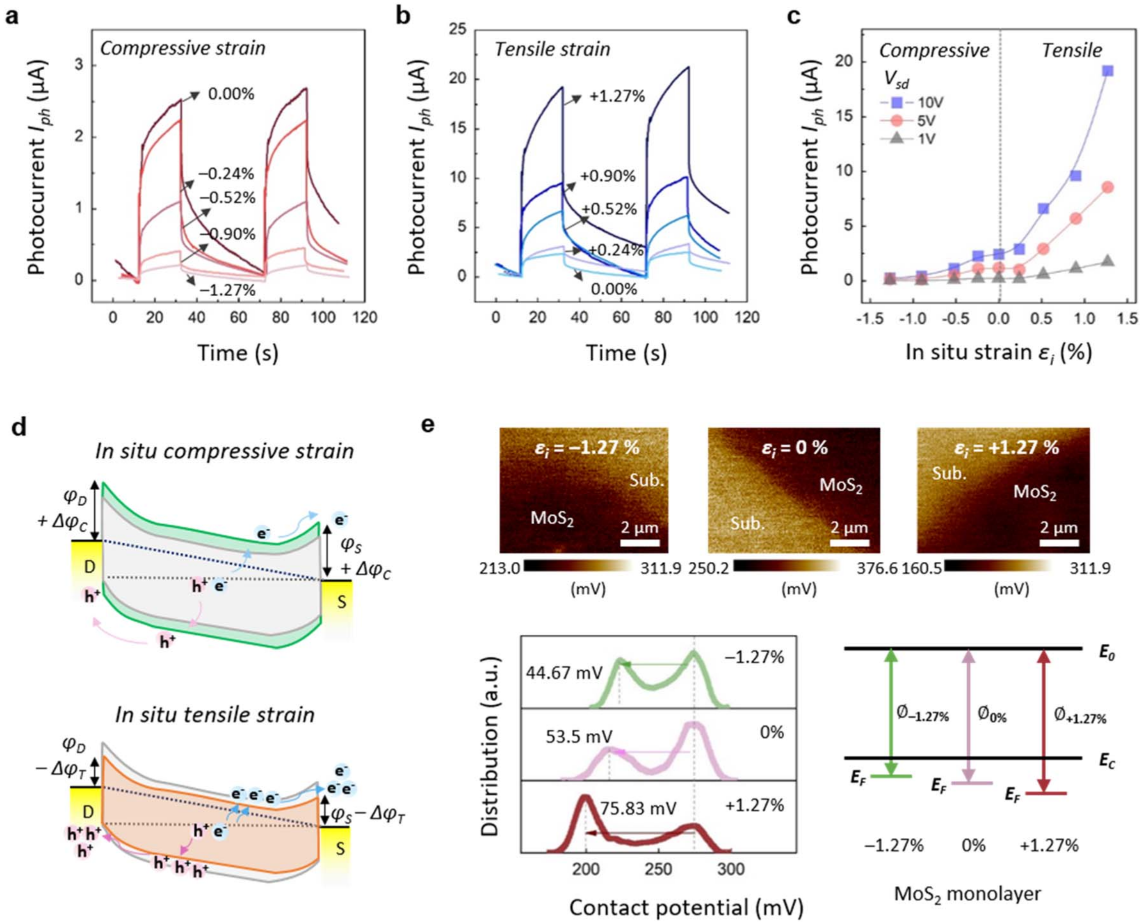

Fig. 2 On/off transient response behaviors of the MoS_2-monolayer-based photodetectors processed with *in situ* (a) compressive and (b) tensile strain ε_i, which were measured at a laser power density P of 259 mW cm^{-2} and $V_{sd} = +10$ V. (c) ε_i-dependent changes in the photocurrent I_{ph} of the strained photodetectors measured at $V_{sd} = +1$, +5, and +10 V. (d) Schematic energy band diagrams of the Au/MoS_2/Au photodetectors, which were adjusted with compressive or tensile strain ε_i in the presence of applied V_{sd} (here, φ_S and φ_D are the Schottky barrier heights of the source and drain contacts, respectively, and $\Delta\varphi_C$ and $\Delta\varphi_T$ are the changes in the barrier height under compressive and tensile ε_i, respectively.) (e) KPFM topography images of the strained MoS_2 films with of $\varepsilon_i = -1.27$, 0, and +1.27%, with contact potential distributions relative to the potential of the bare substrate as a reference. The projected contact potentials of the compressive and tensile strains are presented with the unstrained case for comparison, highlighting the increased work function with the tensile strain and thus the lowered Fermi level.

height with a wider bandgap would induce a smaller photocurrent.

Domain-orientation-dependent photoresponse

To explore the possibility of further increasing the tensile strain level beyond the maximum ε_i of +1.27%, we performed a second post-bending step on the *in situ* strained sample. A total added strain ε_T of +1.80% resulted from convexly post-bending the pre-bent sample with an identical strain level, *i.e.*, post-bending the $\varepsilon_i = +0.90\%$ sample by +0.90%, which was evaluated for all three electrode alignments with respect to the different domain orientations. Fig. 3a and b shows the photocurrent I_{ph} *versus* time at V_{sd} of +10 V at a laser power density of 0.03 mW cm^{-2} before and after applying the post-bending step for the three electrode alignments. Apparently, the I_{ph} values strongly depended on the electrode alignment only in the case of post-bending (Fig. 3b). The maximum I_{ph} values for the θ of 30°-, 15°-, and 0°-domain configurations were very similar at 0.31, 0.31, and 0.32 μA, respectively, before applying the post-bending strain (*i.e.*, the case of $\varepsilon_i \sim +0.9\%$ in Fig. 3a), indicating that the relative electrode positions did not affect the photoresponse with the *in situ* pre-strain. Similarly, on the basis of simulations, changes in the bandgap were reported to be independent of domain orientations in monolayer MoS_2 in the strain range of $\pm 2.0\%$.[43,44]

However, after applying post-bending, the corresponding values changed considerably to 0.38, 0.42, and 0.56 μA, respectively (Fig. 3b). The strong dependency of the domain orientations on the photoresponse with the second bending is related to the piezophototronic effect, wherein the piezoelectricity and thus the polarization field induced by the post-bending cause additional band bending, which acts as an extra driving force for further charge transport. The dependency of angularly positioned electrodes is based on the different levels of dipole moments generated under tensile strain, as exemplified by the cases of the 0° (or 60°) and 30° (or 90°)

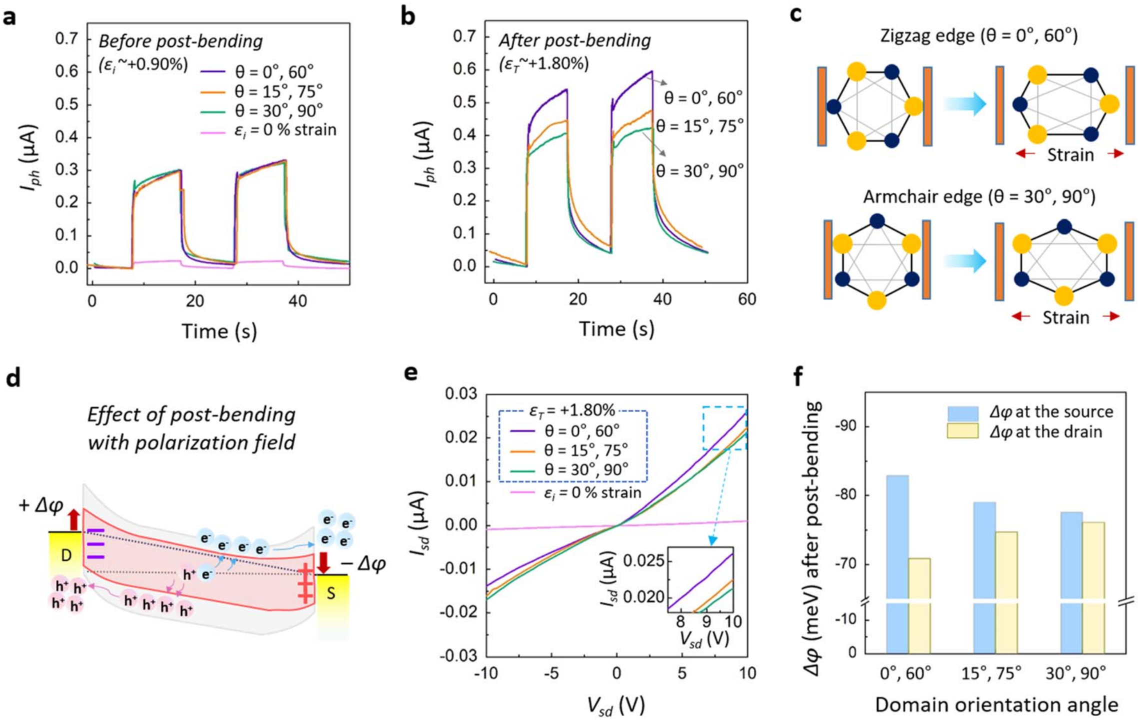

Fig. 3 (a) On/off transient response behaviors of the $\varepsilon_i \sim 0.9\%$-strained photodetectors with adjusted electrode alignment angles of 0° (or 60°), 15° (or 75°), and 30° (or 90°), which were measured at the P of 0.03 mW cm^{-2} and V_{sd} = +10 V. (b) Corresponding response behaviors after applying ε_T of +1.80% by post-bending. (c) Mechanism of piezoelectricity concerning the zigzag-edge and armchair-edge electrode alignments. (d) Schematic of the energy band structure of the double-strained photodetector, reflecting the changes in the barrier height at the source and drain junctions with the marked contributions by polarization potentials at the junctions. Here, $\Delta\varphi$ is the polarization-induced change in the barrier height. (e) I_{sd}–V_{sd} curves of the photodetectors under dark conditions. (f) Estimated relative changes in the Schottky barrier heights at both junctions for the three electrode alignments, in which $\Delta\varphi$ varied depending on the relative domain angles.

adjustments shown in Fig. 3c. The 0° (or 60°) electrode corresponding to the zigzag-edge arrays of alternate Mo and S atoms is believed to create the highest dipole moments with lateral physical extensions, as the relative separation between the centers of anions and cations is maximized, as previously reported.[45,46] Armchair-edge electrodes with 30° (or 90°) domains are the opposite case, *i.e.*, they minimize the creation of dipole moments. A similar dependency of the atomic arrangement on the piezoelectricity of a single-crystal MoS_2 monolayer was previously demonstrated, with a higher piezoelectric coupling strength for the zigzag edge (~300 pC m^{-1}) compared with that for the armchair-edge (~100 pC m^{-1}).[24] Accordingly, a larger polarization field in the 0° (or 60°) electrodes seemed to more effectively produce a higher photoresponse than that in the other two angular electrodes by extending the favorable band bending with adjusted potential barriers at the junctions.[45,46] The extended tensile effect on I_{ph} may also be related to a further reduction in the bandgap, which is responsible for easier charge transport through the junctions.

The changes in the energy band structure after applying the post-bending are schematically illustrated in Fig. 3d. After confirming the thermionic emission conduction through the corresponding plot of $\ln(I_{sd})$–$V_{sd}^{1/4}$ plot (Fig. S12 (ESI†)), the difference in the Schottky barrier height $\Delta\varphi$ after applying post-bending with $\varepsilon_T = +1.80\%$ was estimated using the equation $\Delta\varphi \approx -kT\ln(I_\varepsilon/I_0)$, where k is the Boltzmann constant, T is the temperature, and I_ε and I_0 are the absolute dark currents flowing from the source to the drain with and without the post-bending strain, respectively.[13,36] I_ε and I_0 were extracted from the I_{sd}–V_{sd} curves, which were measured under a total strain of +1.80%, as shown in Fig. 3e. The results of $\Delta\varphi$ are plotted in Fig. 3f for V_{sd} values of −10 and +10 V, indicating the change in barrier height $\Delta\varphi$ at the drain (yellow plots) and source (blue plots) contacts. For example, the resultant $\Delta\varphi$ values for the MoS_2 photodetector with the $\theta \sim 0°$ (or 60°) electrodes were −70.9 and −82.9 meV at the drain and source junctions, respectively. The $\Delta\varphi$ difference of ~12 meV between the drain and source junctions indicates the relatively changed barrier heights induced by the polarization field with the post-bending.[12,36] As expected, the relative changes in $\Delta\varphi$ were reduced to ~4.28 and ~1.46 meV for the $\theta \sim 15°$ (or 75°) and $\theta \sim 30°$ (or 90°) electrodes, respectively, which suggests the strong dependence on polarization field. The energy band schematic in Fig. 3d reflects the altered potential barriers at each junction with the application of polarization field with post-bending.

Ultrahigh-performance double-strained photodetectors

Fig. 4a shows the photodetection performance of the monolayer MoS_2 photodetector with zigzag-edge electrodes processed under the optimized conditions of $\varepsilon_T = +1.80\%$ at $V_{sd} \sim +10$ V

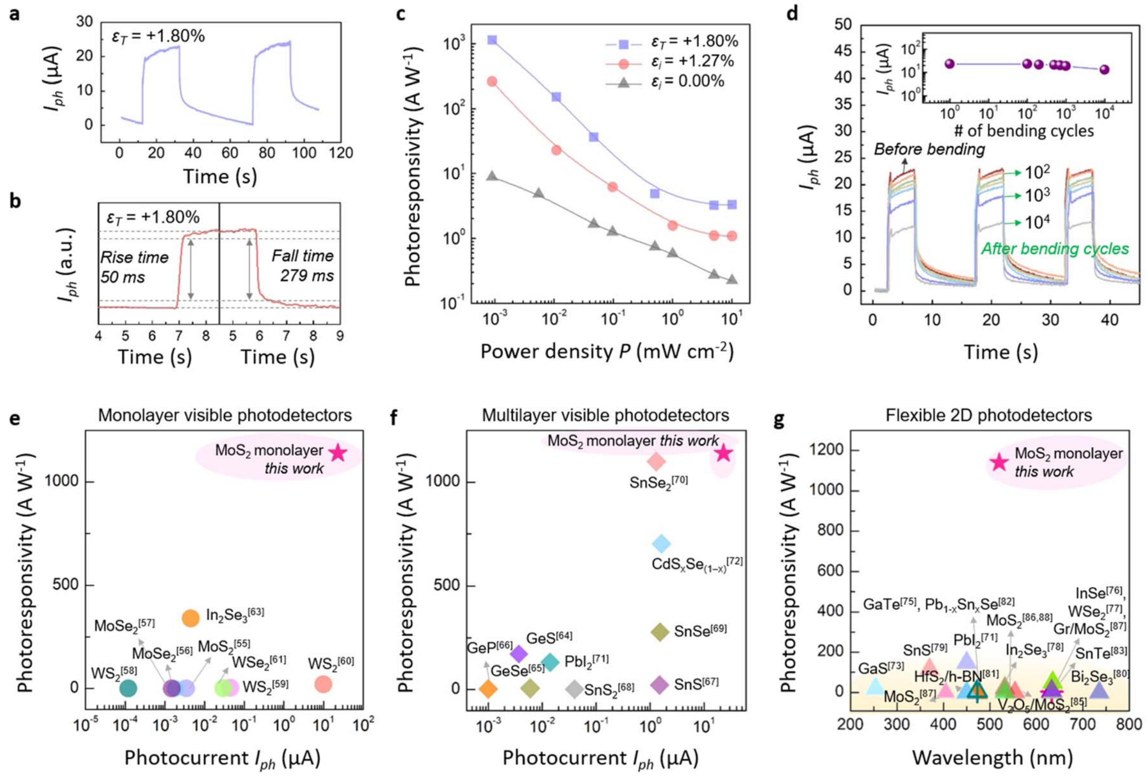

Fig. 4 (a) Transient on/off behavior of I_{ph} in the double-strained photodetector with ε_T of +1.80%, measured at a V_{sd} of +10 V and P of 259 mW cm^{-2}. (b) Rise and fall times (10%-to-90% and 90%-to-10%) of the $\varepsilon_T \sim$ +1.80% photodetector. (c) Variations in photoresponsivity R with increasing power density measured at +10 V under 520 nm irradiation for unstrained and ε_i +1.27%- and ε_T +1.80%-strained photodetectors. (d) Cyclic transient on/off behavior of I_{ph} over 10^4 bending cycles for the double-strained photodetector with ε_T of +1.80%, measured at V_{sd} of +10 V and P of 259 mW cm^{-2} (inset: I_{ph} as a function of the number of cycles). Comparison of our best I_{ph} and R values with the reported ones for (e) monolayer- and (f) multilayer-based 2D visible photodetectors, evincing the outstanding performance of our double-strained photodetector. (g) Comparison of R in flexible 2D photodetector systems. Details on each material in the (e, f and g) charts are provided in Tables S2 and S3.†

and $P \sim 259$ mW cm^{-2}. The highest I_{ph} value of 22.9 μA was achieved by this optimal sample, corresponding to a ~9.5-fold increase relative to the unstrained result (2.4 μA). The rise and fall times were measured, which correspond to the time lapses required for I_{ph} to increase from 10% to 90% of the peak value and to decrease from 90% to 10%, respectively, as shown in Fig. 4b. The obtained rise and fall times of ~50 and ~279 ms, respectively, are quite viable and comparable to those reported for visible-light photodetectors based on MoS_2 monolayers on various substrates, as listed in Table S1 (ESI†), which are even more remarkable when considering our flexible systems using plastic substrates.

The photoresponsivity R was calculated from the relation $R = I_{ph}/(P \times A)$, where P is the incident light power density and A is the active area, based on the I_{sd}–V_{sd} curves shown in Fig. S13 (ESI†). As a result, exceptional R values of 262 and 1142 A W^{-1} were attained with the $\varepsilon_i \sim$ +1.27%- and $\varepsilon_T \sim$ +1.80%-strained samples, respectively, at $P \sim 9 \times 10^{-4}$ mW cm^{-2} and with zigzag-edge electrodes, corresponding to ~29.7- and ~129.3-fold increases with respect to 8.83 A W^{-1} for the unstrained one. Fig. 4c shows the dependency of R on the light power density ranging from 9×10^{-4} to 10.1 mW cm^{-2}, which was measured at V_{sd} = +10 V under 520 nm laser irradiation for the unstrained and $\varepsilon_i \sim$ +1.27%- and $\varepsilon_T \sim$ +1.80%-strained samples with the zigzag-edge electrodes. As expected, R clearly decreased with increasing the power density. The optimal R condition was repeated several times to see the reliability of the highest value of 1142 A W^{-1} as seen in Fig. S14 (ESI†). An average value of 1122.7 (±19.1) A W^{-1} was obtained over the seven different measurements, indicating the fairly good consistency of the photoresponse.

The detectivity D^* was also estimated by considering the noise current density using the equation $D^* = R\sqrt{AB}/i_n$, where A is the active area of the photodetector, B is the bandwidth, and i_n is the noise current.[47,48] The minimum noise current in the frequency range of 1 Hz to 1.6 kHz was extracted from the curves of the noise current density $(i_n/\sqrt{B})$ *versus* frequency as seen in Fig. S15 (ESI†). Note that the noise current density largely depended on the applied *in situ* strain, which was measured under no illumination. A higher noise current density of ~2.05 × 10^{-13} A Hz$^{-1/2}$ was obtained at 1.6 kHz for the +1.27%-strained sample, in contrast to ~7.00 × 10^{-14} and ~2.07 × 10^{-14} A Hz$^{-1/2}$ for the unstrained reference and −1.27%-strained samples, respectively (Fig. S15 (ESI†)). The higher density in the case of tensile strain may be caused primarily by the frequency-independent shot noise that is associated with the favorable junction characteristics determining carrier density.[48] With the consideration of the noise current, the resultant D^* values were 8.9×10^{11} for the unstrained MoS_2 and 9.1×10^{12} Jones ($=$cm Hz$^{1/2}$ W^{-1}) for the +1.27%-strained MoS_2 in the condition of an illumination wavelength of 532 nm and a frequency of 1.6 kHz. The higher R value in the case of tensile strain is surely responsible for the higher D^* value albeit the increased noise current density with the tensile strain. The reported D^* values for various TMD materials ranged from 2.0×10^8 to 7.7×10^{11} Jones (which were measured by the noise current, not by dark current),[49–51] highlighting the promising performance of our device with a D^* value of 9.1×10^{12} Jones. The reported D^* values are listed in Table S2 (ESI†). Note that the detectivity for the +1.80%-strained MoS_2 could not be measured owing to the limitations of our instrument, which could not measure the post-bent samples, although we expect even better detectivity with the additional tensile strain.

Interestingly, a higher ε_T of +2.54% (obtained by combining $\varepsilon_i \sim +1.27\%$ with a post-bending strain of +1.27%) did not result in good photoresponse behavior, as seen in Fig. S16 (ESI†), probably owing to physical incompatibility with the excessive strain, as similarly reported for other 2D materials, which showed limited performance at tensile strains above +1.70%.[52] In the +2.54%-strained MoS_2, the E^1_{2g} peak in the Raman spectra split into E'^- and E'^+ owing to the breakdown of the lattice symmetry, and the A-exciton PL peak did not shift toward a lower photon energy, suggesting potential strain relaxation.[31,53]

Because our photodetectors are based on flexible systems, we extended our evaluation of their photodetection performance by performing up to 10^4 repeated bending cycles. Fig. 4d presents the on/off photocurrent behavior of the optimal photoconductors as cycling proceeded with a bending strain and frequency of 0.9% and 1.3 Hz, respectively, demonstrating that I_{ph} degraded with extended cycling. The peak I_{ph} values are plotted against the number of cycles in the inset of Fig. 4d. After $\sim 10^4$ cycles, I_{ph} apparently decreased by ~42.1%, which is comparable to the reported degradation of ~45.7% in the case of a flexible photodetector composed of monolayer MoS_2 on PET after 10^4 bending cycles.[54]

The best values of the photocurrent and photoresponsivity were projected onto charts comparing various visible photodetectors based on 2D-monolayer or multilayers, as shown in Fig. 4e and f. All values are listed in Table S3 (ESI†) along with information on the material, layer thickness, substrate, and measurement conditions.[55–72] Most of the reported photodetection characteristics were obtained for 2D materials fabricated on rigid Si substrates, with relatively small active areas of a few tens of square micrometers. To the best of our knowledge, the maximum I_{ph} of 22.9 μA and R of 1142 A W^{-1} for the double-strained sample with the zigzag-edge electrodes are the record values among those reported thus far, even with the polymer substrate underlying our monolayer film. The highest reported values in visible photodetectors were ~340 A W^{-1} for In_2Se_3 monolayer (Fig. 4e) and ~1100 A W^{-1} for $SnSe_2$ multilayer (Fig. 4f).[63,70] Fig. 4g additionally compares our maximum R with the reported values exclusively for flexible systems, with the values listed in Table S4 (ESI†).[71,73–88] Our R value far exceeds any reported value, which verifies the excellent performance of our flexible monolayer TMD system incorporating double-strain and domain engineering. The highest value in the flexible system was ~147.6 A W^{-1} for the case of PbI_2 nanosheets.[71] Note that the values used in the comparative charts of Fig. 4e–g were the maximum ones claimed in each reference. Because the R value largely depend on measurement conditions such as P and V_{sd}, the direct comparison may not be indicative of absolute superiority. The P and V_{sd} conditions for each value were given in Tables S3 and S4.†

Conclusions

The combined effects of double-strain engineering and domain engineering were proven to be very effective in producing an ultrahigh photoresponse in centimeter-scale MoS_2-monolayer-film-based photodetectors with symmetric Au electrodes. The unique planar epitaxial grain structure of the monolayer MoS_2 film was enabled by LPCVD utilizing the Na_2S promotor with a *c*-plane sapphire substrate. Using the optimal electrode alignment following the zigzag-edge atomic arrays, the two-step strain engineering enabled record values of $I_{ph} \sim 22.9$ μA and $R \sim 1142$ A W^{-1} at an incident power density of 9×10^{-4} mW cm^{-2} with a maximum tensile strain of +1.80%. Our promising achievements with maximum tensile strain are primarily associated with the combined effects of the direct bandgap (from the monolayer feature), more absorbed photons (thanks to the narrowed bandgap and larger active area), and highly effective charge transport (owing to the altered Schottky barrier heights at the MoS_2–Au interface). In particular, the changes in the potential energy barriers with the tensile strains were estimated from the experimental results; specifically, the Fermi levels were lowered by the first *in situ* strain, and the dark current decreased with the second post-strain. Domain adjustment by positioning the electrodes was understood to be related to modulating dipole moments with respect to atomic arrays, thus determining the polarization field across the electrodes owing to the piezoelectricity of MoS_2.

Experimental

Synthesis of MoS_2 monolayer films

Centimeter-scale monolayer MoS_2 was synthesized on a *c*-plane sapphire substrate using MoO_3 (99.97%, Sigma-Aldrich) and sulfur (99.98%, Sigma-Aldrich) powders *via* LPCVD with the assistance of a Na_2S growth promotor. First, a Na_2S film was prepared by drop-casting a 10.5 mM Na_2S (99.9%, Sigma-Aldrich) solution onto a sapphire substrate at room temperature, followed by annealing at 120 °C. The LPCVD system consisted of two reaction zones designed to vaporize the S powder at 110 °C in the first zone and the MoO_3 powder at 800 °C in the second zone. A vapor pressure of 200 Torr was maintained under Ar gas flowing at 100 sccm. The Na_2S film facing the MoO_3 source in the upper part at a distance of 5 mm was positioned parallel to the bare substrate at a distance of 5 mm.

Fabrication of photodetectors with strain

PMMA (950 PMMA A6, Micro Chem) was spin-coated onto the as-grown MoS_2/sapphire at 3000 rpm for 1 min and annealed at 80 °C for 10 min. The PMMA/MoS_2/sapphire was immersed in a NaOH solution and heated at 85 °C for 10 min. A PET substrate was pre-bent concavely or convexly with a given curvature and fitted into a fixture to maintain the bent state during the transfer of the 2D film. Changing the fixture curvature is the key to modulating the magnitude of strain, and strain ranging from compressive −1.27% to tensile +1.27% was applied. After being separated from the sapphire by floating onto the surface of deionized water, the PMMA/MoS_2 was carefully scooped up by the bent PET substrate. The PMMA/MoS_2/PET sample was then dried on a hot plate at 60 °C for 2 h. The MoS_2/PET was finally secured after removing the PMMA layer by dripping acetone and drying with blowing N_2 gas. After releasing the MoS_2/PET sample from the fixture, it returned to a flat state, in which it was assumed to have residual tensile or compressive strain. Finally, Ni/Au (2 nm/50 nm) was thermally evaporated onto the sides of the transferred MoS_2 film to prepare two-terminal photodetectors. For double-strain engineering, additional strain was imposed by convexly post-bending *in situ* strained photodetectors with +0.90% (or +1.27%) to create a total tensile strain of +1.80% (or +2.54%). For example, the *in situ* strained sample with +0.90% was convexly post-bent with an identical strain of +0.90% for a final total strain of +1.80%.

Characterization and measurement

The Raman and PL spectra of the strained MoS_2 monolayer were recorded using a Raman microscope (inVia RE04, Renishaw) operating at an excitation wavelength of 532 nm. AFM (MultiMode 8, Bruker) was used to characterize the film morphology (including the monolayer thickness) using a commercial Al-coated tip (PPP-CONTR-10, Nanosensors) in contact mode. LFM (Park NX10, Park Systems) images of the synthesized monolayer film were acquired using a cantilever in contact mode, in which the electrical signals were collected with the lateral movement of the cantilever perpendicular to the long axis. HAADF-STEM (JEM-ARM200F, JEOL Ltd) images were corded to reveal the atomic-scale microstructure of the MoS_2 films. The MoS_2 film was transferred onto a Cu grid using the PMMA-assisted transfer method for HAADF-STEM observations. The absorbance and $(\alpha\hbar\nu)^2$ spectra of the strained MoS_2 samples were recorded using a UV-visible spectrophotometer (V-750, Jasco). Electrical and optical measurements were carried out using an I–V analyzer (4200A-SCS Parameter Analyzer, Keithley) and a probe station (MST 8000C, MS TECH) under illumination using a 532 nm (MGL-III, Uniotech) or 520 nm (MLL-III-520 L, CNI Laser) laser source at power densities ranging from 0.0009 to 259 mW cm^{-2}. The switching and sweep (I_{sd}–V_{sd}) curves of the fabricated MoS_2 photodetectors were recorded under ambient conditions. The noise current density was measured under dark conditions at $V_{sd} \sim +1$ V in the frequency range of 1 Hz to 1.6 kHz with a frequency resolution of 1 Hz using a dynamic signal analyzer (Agilent 35670A, Keysight) equipped with a preamplifier (428, Keithley).

Author contributions

Y. S. J. fabricated and characterized the samples and wrote the manuscript, with inputs from all the authors. J. W. P., J. Y. K., Y. P., and D. G. R. participated in the characterization. J. H. and J. H. C. supervised the work. Y. S. C. guided this research and completed the manuscript.

Conflicts of interest

The authors declare no conflict of interest.

Acknowledgements

This work was financially supported by grants from the National Research Foundation of Korea (NRF-2020M3D1A2102913 and NRF-2021R1A2C2013501) and the Creative Materials Discovery Program of the Ministry of Science and ICT (2018M3D1A1058536).

References

1 Y. Li, N. Li, S. Zhao, J. Fan and J. J. Kai, *J. Mater. Chem. A*, 2020, **8**, 760–769.
2 D. B. Kim, J. W. Lee and Y. S. Cho, *Adv. Funct. Mater.*, 2021, **31**, 2007131.
3 Y. S. Jung, H. J. Choi, J. W. Park and Y. S. Cho, *Nano Energy*, 2021, **82**, 105690.
4 R. Samal, G. Sanyal, B. Chakraborty and C. S. Rout, *J. Mater. Chem. A*, 2021, **9**, 2560–2591.
5 Q. Li, J. Meng and Z. Li, *J. Mater. Chem. A*, 2022, **10**, 8107–8128.
6 J. W. Park, Y. S. Jung, S. H. Park, H. J. Choi and Y. S. Cho, *Adv. Opt. Mater.*, 2022, **10**, 2200898.
7 H. J. Choi, Y. S. Jung, S. M. Lee, S. Kang, D. Seo, H. Kim, H. J. Choi, G. H. Lee and Y. S. Cho, *Cryst. Growth Des.*, 2020, **20**, 2698–2705.
8 S. Deng, A. V. Sumant and V. Berry, *Nano Today*, 2018, **22**, 14–35.
9 C. Cui, F. Xue, W. J. Hu and L. J. Li, *npj 2D Mater. Appl.*, 2018, **2**, 18.
10 J. Lu, J. Yao, J. Yan, W. Gao, L. Huang, Z. Zheng, M. Zhang and J. Li, *Mater. Horiz.*, 2020, **7**, 1427–1435.
11 Y. Peng, M. Que, J. Tao, X. Wang, J. Lu, G. Hu, B. Wan, Q. Xu and C. Pan, *2D Mater.*, 2018, **5**, 042003.
12 P. Gant, P. Huang, D. Pérez de Lara, D. Guo, R. Frisenda and A. Castellanos-Gomez, *Mater. Today*, 2019, **27**, 8–13.
13 W. Wu, L. Wang, R. Yu, Y. Liu, S. Wei, J. Hone and Z. L. Wang, *Adv. Mater.*, 2016, **28**, 8463–8468.
14 P. Kang, M. C. Wang, P. M. Knapp and S. W. Nam, *Adv. Mater.*, 2016, **28**, 4639–4645.
15 Q. Zhang, Z. Chang, G. Xu, Z. Wang, Y. Zhang, Z. Xu, S. Chen, Q. Bao, J. Z. Liu, Y. Mai, W. Duan, M. S. Fuhrer and C. Zheng, *Adv. Funct. Mater.*, 2016, **26**, 8707–8714.
16 S. Pak, J. Lee, Y. Lee, A. Jang, S. Ahn, K. Y. Ma, Y. Cho, J. Hong, S. Lee, H. Y. Jeong, H. Im, H. S. Shin,

S. M. Morris, S. Cha, J. I. Sohn and J. M. Kim, *Nano Lett.*, 2017, **17**, 5634–5640.

17 R. Schmidt, I. Niehues, R. Schneider, M. Drüppel, T. Deilmann, M. Rohlfing, S. M. De Vasconcellos, A. Castellanos-Gomez and R. Bratschitsch, *2D Mater.*, 2016, **3**, 021011.

18 I. Niehues, R. Schmidt, M. Drüppel, P. Marauhn, D. Christiansen, M. Selig, G. Berghäuser, D. Wigger, R. Schneider, L. Braasch, R. Koch, A. Castellanos-Gomez, T. Kuhn, A. Knorr, E. Malic, M. Rohlfing, S. Michaelis De Vasconcellos and R. Bratschitsch, *Nano Lett.*, 2018, **18**, 1751–1757.

19 A. Castellanos-Gomez, R. Roldán, E. Cappelluti, M. Buscema, F. Guinea, H. S. J. Van Der Zant and G. A. Steele, *Nano Lett.*, 2013, **13**, 5361–5366.

20 W. Li, M. Dai, Y. Hu, H. Chen, X. Zhu, Q. Yang and P. Hu, *ACS Appl. Mater. Interfaces*, 2019, **11**, 47098–47105.

21 F. Li, T. Shen, L. Xu, C. Hu and J. Qi, *Adv. Electron. Mater.*, 2019, **5**, 1900803.

22 K. Zhang, J. Zhai and Z. L. Wang, *2D Mater.*, 2018, **5**, 035038.

23 W. Wu, L. Wang, Y. Li, F. Zhang, L. Lin, S. Niu, D. Chenet, X. Zhang, Y. Hao, T. F. Heinz, J. Hone and Z. L. Wang, *Nature*, 2014, **514**, 470–474.

24 H. Zhu, Y. Wang, J. Xiao, M. Liu, S. Xiong, Z. J. Wong, Z. Ye, Y. Ye, X. Yin and X. Zhang, *Nat. Nanotechnol.*, 2015, **10**, 151–155.

25 S. K. Kim, R. Bhatia, T. H. Kim, D. Seol, J. H. Kim, H. Kim, W. Seung, Y. Kim, Y. H. Lee and S. W. Kim, *Nano Energy*, 2016, **22**, 483–489.

26 Y. S. Jung, H. J. Choi, S. H. Park, D. Kim, S. Park and Y. S. Cho, *Small*, 2022, **18**, 2200184.

27 X. Xu, T. Schultz, Z. Qin, N. Severin, B. Haas, S. Shen, J. N. Kirchhof, A. Opitz, C. T. Koch, K. Bolotin, J. P. Rabe, G. Eda and N. Koch, *Adv. Mater.*, 2018, **30**, 1803748.

28 J. Ludwig, A. N. Mehta, M. Mascaro, U. Celano, D. Chiappe, H. Bender, W. Vandervorst and K. Paredis, *Nanotechnology*, 2019, **30**, 285705.

29 X. Zhang, T. H. Choudhury, M. Chubarov, Y. Xiang, B. Jariwala, F. Zhang, N. Alem, G. Wang, J. A. Robinson and J. M. Redwing, *Nano Lett.*, 2018, **18**, 1049–1056.

30 T. Li, W. Guo, L. Ma, W. Li, Z. Yu, Z. Han, S. Gao, L. Liu, D. Fan, Z. Wang, Y. Yang, W. Lin, Z. Luo, X. Chen, N. Dai, X. Tu, D. Pan, Y. Yao, P. Wang, Y. Nie, J. Wang, Y. Shi and X. Wang, *Nat. Nanotechnol.*, 2021, **16**, 1201–1207.

31 H. J. Conley, B. Wang, J. I. Ziegler, R. F. Haglund, S. T. Pantelides and K. I. Bolotin, *Nano Lett.*, 2013, **13**, 3626–3630.

32 H. J. Choi, W. Jang, B. C. Mohanty, Y. S. Jung, A. Soon and Y. S. Cho, *J. Phys. Chem. Lett.*, 2018, **9**, 5934–5939.

33 M. N. H. Mia, M. F. Pervez, M. K. Hossain, M. Reefaz Rahman, M. J. Uddin, M. A. Al Mashud, H. K. Ghosh and M. Hoq, *Results Phys.*, 2017, **7**, 2683–2691.

34 R. Ahmad, R. Srivastava, S. Yadav, D. Singh, G. Gupta, S. Chand and S. Sapra, *J. Phys. Chem. Lett.*, 2017, **8**, 1729–1738.

35 K. F. Mak, C. Lee, J. Hone, J. Shan and T. F. Heinz, *Phys. Rev. Lett.*, 2010, **105**, 136805.

36 J. Qi, Y. W. Lan, A. Z. Stieg, J. H. Chen, Y. L. Zhong, L. J. Li, C. D. Chen, Y. Zhang and K. L. Wang, *Nat. Commun.*, 2015, **6**, 7430.

37 O. Lopez-Sanchez, D. Lembke, M. Kayci, A. Radenovic and A. Kis, *Nat. Nanotechnol.*, 2013, **8**, 497–501.

38 J. Kwon, Y. K. Hong, G. Han, I. Omkaram, W. Choi, S. Kim and Y. Yoon, *Adv. Mater.*, 2015, **27**, 2224–2230.

39 C. Kim, I. Moon, D. Lee, M. S. Choi, F. Ahmed, S. Nam, Y. Cho, H. J. Shin, S. Park and W. J. Yoo, *ACS Nano*, 2017, **11**, 1588–1596.

40 J. R. Durán Retamal, D. Periyanagounder, J. J. Ke, M. L. Tsai and J. H. He, *Chem. Sci.*, 2018, **9**, 7727–7745.

41 W. Yu, S. Li, Y. Zhang, W. Ma, T. Sun, J. Yuan, K. Fu and Q. Bao, *Small*, 2017, **13**, 1700268.

42 M. Tosun, D. Fu, S. B. Desai, C. Ko, J. Seuk Kang, D. Lien, M. Najmzadeh, S. Tongay, J. Wu and A. Javey, *Sci. Rep.*, 2015, **5**, 10990.

43 P. Lu, X. Wu, W. Guo and X. C. Zeng, *Phys. Chem. Chem. Phys.*, 2012, **14**, 13035–13040.

44 Dimple, N. Jena, S. D. Behere and A. De Sarkar, *Pramana*, 2017, **89**, 2.

45 S. M. Lee, W. Jang, B. C. Mohanty, J. Yoo, J. W. Jang, D. B. Kim, Y. Yi, A. Soon and Y. S. Cho, *Chem. Mater.*, 2018, **30**, 7776–7781.

46 Y. Li, T. Wang, M. Wu, T. Cao, Y. Chen, R. Sankar, R. K. Ulaganathan, F. Chou, C. Wetzel, C. Xu, S. G. Louie and S. Shi, *2D Mater.*, 2018, **5**, 021002.

47 J. Jiang, X. Zou, Y. Lv, Y. Liu, W. Xu, Q. Tao, Y. Chai and L. Liao, *Nat. Commun.*, 2020, **11**, 1–9.

48 D. B. Kim, J. Han, Y. S. Jung, K. S. Park, Y. S. Park, J. S. Heo and Y. S. Cho, *Mater. Horiz.*, 2022, **9**, 1207–1215.

49 C. Li, J. Zhu, W. Du, Y. Huang, H. Xu, Z. Zhai and G. Zou, *Nanoscale Res. Lett.*, 2021, **16**, 123.

50 D. Kufer and G. Konstantatos, *Nano Lett.*, 2015, **15**, 7307–7313.

51 Q. Liang, Q. Wang, Q. Zhang, J. Wei, S. X. Lim, R. Zhu, J. Hu, W. Wei, C. Lee, C. Sow, W. Zhang and A. T. S. Wee, *Adv. Mater.*, 2019, **31**, 1807609.

52 Z. Li, Y. Lv, L. Ren, J. Li, L. Kong, Y. Zeng, Q. Tao, R. Wu, H. Ma, B. Zhao, D. Wang, W. Dang, K. Chen, L. Liao, X. Duan, X. Duan and Y. Liu, *Nat. Commun.*, 2020, **11**, 1151.

53 S. B. Desai, G. Seol, J. S. Kang, H. Fang, C. Battaglia, R. Kapadia, J. W. Ager, J. Guo and A. Javey, *Nano Lett.*, 2014, **14**, 4592–4597.

54 S. Pak, S. Jang, T. Kim, J. Lim, J. S. Hwang, Y. Cho, H. Chang, A. Jang, K. Park, J. Hong and S. Cha, *Adv. Mater.*, 2021, **33**, 2102091.

55 Z. Yin, H. Li, H. Li, L. Jiang, Y. Shi, Y. Sun, G. Lu, Q. Zhang, X. Chen and H. Zhang, *ACS Nano*, 2012, **6**, 74–80.

56 J. Xia, X. Huang, L. Z. Liu, M. Wang, L. Wang, B. Huang, D. D. Zhu, J. J. Li, C. Z. Gu and X. M. Meng, *Nanoscale*, 2014, **6**, 8949–8955.

57 Y. H. Chang, W. Zhang, Y. Zhu, Y. Han, J. Pu, J. K. Chang, W. T. Hsu, J. K. Huang, C. L. Hsu, M. H. Chiu, T. Takenobu, H. Li, C. I. Wu, W. H. Chang, A. T. S. Wee and L. J. Li, *ACS Nano*, 2014, **8**, 8582–8590.

58 C. Lan, C. Li, Y. Yin and Y. Liu, *Nanoscale*, 2015, **7**, 5974–5980.

59 Y. Chen, L. Gan, H. Li, Y. Ma, T. Zhai, Y. Chen, L. Gan, H. Q. Li, Y. Ma and T. Y. Zhai, *Adv. Mater.*, 2017, **29**, 1603550.

60 Y. Fan, Y. Zhou, X. Wang, H. Tan, Y. Rong, J. H. Warner, Y. Fan, Y. Zhou, X. Wang, H. Tan, Y. Rong and J. H. Warner, *Adv. Opt. Mater.*, 2016, **4**, 1573–1581.

61 J. Chen, B. Liu, Y. Liu, W. Tang, C. T. Nai, L. Li, J. Zheng, L. Gao, Y. Zheng, H. S. Shin, H. Y. Jeong and K. P. Loh, *Adv. Mater.*, 2015, **27**, 6722–6727.

62 S. Yang, S. Tongay, Y. Li, Q. Yue, J. B. Xia, S. S. Li, J. Li and S. H. Wei, *Nanoscale*, 2014, **6**, 7226–7231.

63 J. Zhou, Q. Zeng, D. Lv, L. Sun, L. Niu, W. Fu, F. Liu, Z. Shen, C. Jin and Z. Liu, *Nano Lett.*, 2015, **15**, 6400–6405.

64 P. Ramasamy, D. Kwak, D. H. Lim, H. S. Ra and J. S. Lee, *J. Mater. Chem. C*, 2016, **4**, 479–485.

65 J. Liu, Y. Zhou, Y. Lin, M. Li, H. Cai, Y. Liang, M. Liu, Z. Huang, F. Lai, F. Huang and W. Zheng, *ACS Appl. Mater. Interfaces*, 2019, **11**, 4123–4130.

66 L. Li, W. Wang, P. Gong, X. Zhu, B. Deng, X. Shi, G. Gao, H. Li and T. Zhai, *Adv. Mater.*, 2018, **30**, 1706771.

67 G. Liu, Y. Li, B. Li, H. Tian, C. Fan, Y. Zhang, Z. Hua, M. Wang, H. Zheng and E. Li, *J. Mater. Chem. C*, 2018, **6**, 10036–10041.

68 J. Xia, D. Zhu, L. Wang, B. Huang, X. Huang and X. Meng, *Adv. Funct. Mater.*, 2015, **25**, 4255–4261.

69 L. Hao, Y. Du, Z. Wang, Y. Wu, H. Xu, S. Dong, H. Liu, Y. Liu, Q. Xue, Z. Han, K. Yan and M. Dong, *Nanoscale*, 2020, **12**, 7358–7365.

70 X. Zhou, L. Gan, W. Tian, Q. Zhang, S. Jin, H. Li, Y. Bando, D. Golberg and T. Zhai, *Adv. Mater.*, 2015, **27**, 8035–8041.

71 M. Zhong, L. Huang, H. X. Deng, X. Wang, B. Li, Z. Wei and J. Li, *J. Mater. Chem. C*, 2016, **4**, 6492–6499.

72 J. Xia, Y. X. Zhao, L. Wang, X. Z. Li, Y. Y. Gu, H. Q. Cheng and X. M. Meng, *Nanoscale*, 2017, **9**, 13786–13793.

73 P. Hu, L. Wang, M. Yoon, J. Zhang, W. Feng, X. Wang, Z. Wen, J. C. Idrobo, Y. Miyamoto, D. B. Geohegan and K. Xiao, *Nano Lett.*, 2013, **13**, 1649–1654.

74 Y. Zhou, Y. Zhou, Y. Nie, Y. Liu, K. Yan, J. Hong, C. Jin, J. Yin, Z. Liu and H. Peng, *ACS Nano*, 2014, **8**, 1485–1490.

75 Z. Wang, M. Safdar, M. Mirza, K. Xu, Q. Wang, Y. Huang, F. Wang, X. Zhan and J. He, *Nanoscale*, 2015, **7**, 7252–7258.

76 S. R. Tamalampudi, Y. Y. Lu, U. R. Kumar, R. Sankar, C. Liao, B. K. Moorthy, C. H. Cheng, F. C. Chou and Y. T. Chen, *Nano Lett.*, 2014, **14**, 2800–2806.

77 Z. Zheng, T. Zhang, J. Yao, Y. Zhang, J. Xu and G. Yang, *Nanotechnology*, 2016, **27**, 225501.

78 D. Wang, Y. Lu, J. Meng, X. Zhang, Z. Yin, M. Gao, Y. Wang, L. Cheng, J. You and J. Zhang, *J. Mater. Chem. C*, 2016, **4**, 8094–8103.

79 J. Yao, G. Yang, J. Yao and G. Yang, *Small*, 2018, **14**, 1704524.

80 J. L. Liu, H. Chen, X. Li, H. Wang, Z. K. Zhang, W. W. Pan, G. Yuan, C. L. Yuan, Y. L. Ren and W. Lei, *J. Alloys Compd.*, 2020, **818**, 152819.

81 D. Wang, Y. Lu, J. Meng, X. Zhang, Z. Yin, M. Gao, Y. Wang, L. Cheng, J. You and J. Zhang, *Nanoscale*, 2019, **11**, 9310–9318.

82 Q. Wang, K. Xu, Z. Wang, F. Wang, Y. Huang, M. Safdar, X. Zhan, F. Wang, Z. Cheng and J. He, *Nano Lett.*, 2015, **15**, 1183–1189.

83 J. Yang, W. Yu, Z. Pan, Q. Yu, Q. Yin, L. Guo, Y. Zhao, T. Sun, Q. Bao and K. Zhang, *Small*, 2018, **14**, 1802598.

84 H. Xu, J. Wu, Q. Feng, N. Mao, C. Wang and J. Zhang, *Small*, 2014, **10**, 2300–2306.

85 P. Sahatiya, C. S. K. Reddy and S. Badhulika, *J. Mater. Chem. C*, 2017, **5**, 12728–12736.

86 K. Zhang, M. Peng, A. Yu, Y. Fan, J. Zhai and Z. L. Wang, *Mater. Horiz.*, 2019, **6**, 826–833.

87 T. Y. Kim, J. Ha, K. Cho, J. Pak, J. Seo, J. Park, J. K. Kim, S. Chung, Y. Hong and T. Lee, *ACS Nano*, 2017, **11**, 10273–10280.

88 F. Yu, M. Hu, F. Kang and R. Lv, *Prog. Nat. Sci.: Mater. Int.*, 2018, **28**, 563–568.